

A convective fluid pendulum revealing states of order and chaos

Jinzi Mac Huang^{1,2*} and Nicholas J. Moore^{3†}

1. NYU-ECNU Institute of Physics and Institute of Mathematical Sciences,
New York University Shanghai, Shanghai, 200122, China

2. Applied Math Lab, Courant Institute, New York University, New York, NY 10012, USA

3. Department of Mathematics, Colgate University, Hamilton, NY 13346, USA

(Dated: July 27, 2023)

We examine thermal convection in a two-dimensional annulus using fully resolved direct numerical simulation (DNS) in conjunction with a low-dimensional model deriving from Galerkin truncation of the governing Navier-Stokes Boussinesq (NSB) equations. The DNS is based on fast and accurate pseudo-spectral discretization of the full NSB system with implicit-explicit time stepping. Inspired by the numerical results, we propose a reduced model that is based on a Fourier-Laurent truncation of the NSB system and can generalize to any degree of accuracy. We demonstrate that the lowest-order model capable of satisfying all boundary conditions on the annulus successfully captures reversals of the large-scale circulation (LSC) in certain regimes. Based on both the DNS and stability analysis of the reduced model, we identify a sequence of transitions between (i) a motionless conductive state, (ii) a state of steady circulation, (iii) non-periodic dynamics and chaotic reversals of the LSC, (iv) a high Rayleigh-number state in which LSC reversals are periodic despite turbulent fluctuations at the small scale. The reduced model reveals a link to a damped pendulum system with a particular form of external forcing. The oscillatory pendulum motion provides an accurate prediction for the LSC reversal frequency in the high Rayleigh-number regime.

I. INTRODUCTION

The nonlinear coupling between temperature and flow fields in thermal convection leads to a range of highly nontrivial dynamics [1–6]. For example, the collective motion of a turbulent flow may form a large-scale circulation (LSC) that can drive atmospheric and oceanic patterns [7, 8]. The direction of the LSC is known to reverse [9, 10], which can lead to observable effects such as a sudden changes in wind direction [11]. Reversals of the LSC in mantle convection may even play a role in reversals of Earth’s magnetic dipole [12], and in solar convection the magnetic switchbacks of the Sun [13]. In other contexts, the mixing of moving fluids can substantially enhance heat transfer rates [4, 14–18], making fluids perfect coolants. It is even more interesting when thermal convection couples to a moving interface, where processes like melting [19–21], erosion [22–27], dissolution [28–31], and sublimation [32, 33] are accelerated by convection as solid morphology evolves. On an extremely large scale, convection in the Earth’s mantle drives plate tectonics [34–37].

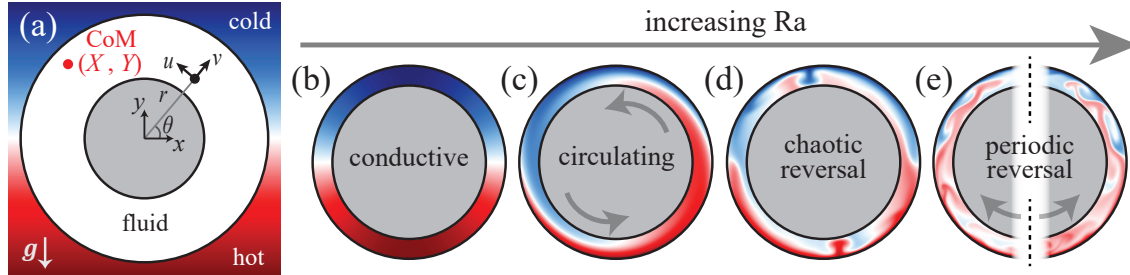


FIG. 1. Thermal convection in an annulus. (a) Schematic showing the fluid domain $[r \in (r_0, 1/2)]$ as an annulus embedded in a solid with constant vertical temperature gradient. (b) At low Ra , the fluid stays motionless and heat simply conducts through the fluid. (c) Increasing Ra beyond a critical value leads to circulating fluid motion. (d) Further increasing Ra leads to chaotic circulations that switch direction randomly. (e) At very high Ra , the reversal motion becomes periodic while the small-scale flow is turbulent. Movies of (b)-(e) are included in the Supplemental Material. Rayleigh-number values are $Ra = 1.4 \times 10^5$ (b), 3.1×10^6 (c), 2.5×10^7 (d), and 1.1×10^9 (e). In all cases, $Pr = 4$ and $r_0 = 0.4$.

In this manuscript and companion letter [38], we consider a canonical example of two-dimensional (2D) thermal convection shown in Fig. 1(a) [39], in which an annular domain of fluid is heated from below. Depending on the strength of the thermal forcing, the fluid may remain motionless in a conductive state [Fig. 1(b)], circulate steadily in either the clockwise (CW) or counter-clockwise (CCW) direction [Fig. 1(c)], or exhibit reversals of the LSC, be they chaotic [Fig. 1(d)] or

* machuang@nyu.edu; The authors contributed equally.

† nickmoore83@gmail.com; The authors contributed equally.

periodic [Fig. 1(e)]. The circulatory nature of thermal convection, which appears generically across many settings, is especially reinforced by the annular shape of the domain considered here. The feedback with geometry tends to create a single, dominant convection cell, while minimizing other effects, such as corner rolls or detached plumes [9, 40, 41]. This large convection cell represents large-scale coherent motion observed at high Rayleigh number in other geometries and in other applications [4, 9, 10, 42, 43].

Previous studies have qualitatively linked the rich dynamics in Fig. 1 to the famous Lorenz system [44–46], a dynamical system describing thermal convection in a planar domain. Diverse states with order and chaos have been observed in both models [44, 45, 47] and experiments [48, 49]. Phenomenological models developed for other geometries lend additional insight [9, 10, 41]. However, a precise model for annular convection that derives systematically from the governing equations and that quantitatively predicts the sequence of transitions is still missing. In this work, we revisit this classic configuration of thermal convection and analytically derive a low-dimensional model from the flow and heat equations. By studying the time evolution of the fluid center of mass (CoM) and the angular momentum L , our work links the thermal convection in Fig. 1 to a mechanical pendulum problem for CoM and provides analytic predictions of the onset of fluid motion and chaos.

In the following, we introduce the governing equations (Sec. II), and then discuss a scheme to perform direct numerical simulations of thermal convection (Sec. III). We next link the observed nonlinear behaviors to a low-dimensional system of ordinary differential equations (ODEs) (Sec. IV). The derivation of this dynamical system requires minimal assumptions, and it recovers the numerical observations over a large range of parameters. Through analyzing the critical states and stability of the ODE system, the transition between different dynamical states can be analyzed in detail (Sec. V). We finally show how the high Rayleigh-number convection can be linked to a mechanical pendulum (Sec. VI), and close with some concluding remarks (Sec. VII).

II. GOVERNING EQUATIONS

Consider an annular fluid domain of inner radius R_0 , outer radius R_1 , and height $h = 2R_1$ as depicted in Fig. 1(a). The fluid is heated from below, with temperature difference ΔT between the bottom and top of the annulus. Material properties include the kinematic viscosity ν , the thermal diffusivity κ , the thermal expansion coefficient β_T , and the average fluid density ρ_0 . The coupled fluid flow and heat transport inside the annulus are governed by the incompressible Navier-Stokes equations with Boussinesq approximation (NSB):

$$\frac{\partial \mathbf{u}}{\partial t} + \mathbf{u} \cdot \nabla \mathbf{u} = -\nabla p + \text{Pr} \nabla^2 \mathbf{u} + \text{Pr} \text{Ra} T \mathbf{e}_y, \quad (1)$$

$$\frac{\partial T}{\partial t} + \mathbf{u} \cdot \nabla T = \nabla^2 T, \quad (2)$$

$$\nabla \cdot \mathbf{u} = 0. \quad (3)$$

The above equations are in dimensionless form, with space scaled on h , time on h^2/κ (the thermal diffusive timescale), velocity on κ/h , and density variations on $\Delta\rho = \rho_0\beta_T\Delta T$. Variables include the dimensionless velocity \mathbf{u} , pressure p , and temperature T fields. Equations (1) to (3) represent conservation of momentum, thermal transport, and incompressibility respectively. Dimensionless parameters include the Rayleigh number Ra and the Prandtl number Pr :

$$\text{Ra} = \frac{\beta_T \Delta T h^3 g}{\nu \kappa}, \quad \text{Pr} = \frac{\nu}{\kappa}. \quad (4)$$

The Rayleigh number measures the relative strength of thermal forcing, while the Prandtl number measures the ratio of momentum to thermal diffusivity.

The imposed temperature on the outer boundary of the annulus decreases linearly with height, while the inner boundary remains adiabatic. Meanwhile, the velocity field, expressed as $\mathbf{u} = u\mathbf{e}_\theta + v\mathbf{e}_r$ in polar coordinates, satisfies no-slip conditions on both boundaries. The boundary conditions are thus:

$$u = v = 0 \quad \text{at } r = r_0 \text{ and } r = 1/2, \quad (5)$$

$$\frac{\partial T}{\partial r} = 0 \quad \text{at } r = r_0, \quad (6)$$

$$T = \frac{1 - \sin \theta}{2} \quad \text{at } r = 1/2. \quad (7)$$

Due to our nondimensionalization, $r = 1/2$ represents the outer boundary and $r = r_0 = R_0/2R_1$ the inner boundary. In Eqs. (1) to (7), the three dimensionless numbers $\text{Ra}, \text{Pr}, r_0$ serve as the control parameters.

We first note that system Eqs. (1)–(7) supports a conductive state in which the temperature decreases with height and no fluid motion occurs. By setting $\mathbf{u} = 0$ in Eq. (2) and satisfying boundary conditions Eqs. (6) and (7), the conductive-state

temperature distribution can be determined in exact form as

$$T_{\text{cond}} = \frac{1}{2} - \frac{r_0}{1 + 4r_0^2} \left(\frac{r}{r_0} + \frac{r_0}{r} \right) \sin \theta. \quad (8)$$

In this state, relatively cool, heavy fluids sits atop warm, light fluid, thus raising the center of mass (CoM). Notice that, as a consequence of the inner adiabatic condition, the temperature within the fluid does not simply vary *linearly* with height. The dimensionless coordinates of the CoM are given by

$$X = -\frac{1}{A_0} \int_{\Omega} x T dA, \quad Y = -\frac{1}{A_0} \int_{\Omega} y T dA. \quad (9)$$

where $A_0 = \pi(1 - 4r_0^2)/4$ is the area of the annulus and $dA = r dr d\theta$ is the area element. We note that the dimensional CoM can be obtained by multiplying by $h\beta_T \Delta T$. Inserting (8) into (9) and integrating, gives the height of the conductive-state CoM,

$$y_0 = \frac{1 + 12r_0^2}{16(1 + 4r_0^2)}. \quad (10)$$

From this formula, it is clear that $y_0 > 0$ for any value of r_0 , thus confirming that the conductive-state CoM lies above the center of the annulus.

At sufficiently high Rayleigh number, the top-heavy conductive state gives way to thermal convection. The circulatory nature of thermal convection, which appears generically across many settings, is especially reinforced here by the annular shape of the domain. This feedback with geometry tends to create a dominant convection cell that fits the annulus, although fine-grained, complex dynamics may appear in combination. To characterize the leading-order dynamics, we introduce the *average angular momentum* L of the fluid

$$L = \frac{1}{A_0} \int_0^{2\pi} \int_{r_0}^{1/2} r^2 u dr d\theta. \quad (11)$$

Here, $L > 0$ corresponds to rotation in the counter-clockwise (CCW) direction.

III. DIRECT NUMERICAL SIMULATIONS

In this section, we discuss direct numerical simulation (DNS) of the NSB system given by Eqs. (1) to (7). We first introduce the numerical methods and then discuss results of the simulations.

A. Numerical methods

Our simulation method is based on the 2D streamfunction-vorticity form of Eqs. (1) to (3):

$$\frac{\partial \omega}{\partial t} + \mathbf{u} \cdot \nabla \omega = \text{Pr} \nabla^2 \omega + \text{Pr Ra} \left(\frac{\partial T}{\partial r} \cos \theta - \frac{1}{r} \frac{\partial T}{\partial \theta} \sin \theta \right), \quad (12)$$

$$\frac{\partial T}{\partial t} + \mathbf{u} \cdot \nabla T = \nabla^2 T, \quad (13)$$

$$-\nabla^2 \psi = \omega, \quad \mathbf{u} = \nabla_{\perp} \psi. \quad (14)$$

Rather than solving for \mathbf{u} and p , our method solves for the vorticity $\omega = r^{-1} [\partial_r(ru) - \partial_{\theta}v]$ and stream function ψ . Velocity can then be recovered as $\mathbf{u} = \nabla_{\perp} \psi = r^{-1} \psi_{\theta} \mathbf{e}_r - \psi_r \mathbf{e}_{\theta}$, so $u = -\psi_r$ and $v = r^{-1} \psi_{\theta}$.

We first discretize time with the second-order Adam-Bashforth Backward Differentiation method (ABBD2). At time step $t = n\Delta t$, Eqs. (12) to (14) become

$$\nabla^2 \omega^{(n)} - \sigma_1 \omega^{(n)} = f^{(n)}, \quad (15)$$

$$\nabla^2 T^{(n)} - \sigma_2 T^{(n)} = g^{(n)}, \quad (16)$$

$$-\nabla^2 \psi^{(n)} = \omega^{(n)}, \quad (17)$$

where

$$\nabla^2 = \frac{\partial^2}{\partial r^2} + \frac{1}{r} \frac{\partial}{\partial r} + \frac{1}{r^2} \frac{\partial^2}{\partial \theta^2}, \quad \sigma_1 = \frac{3}{2 \text{Pr} \Delta t}, \quad \sigma_2 = \frac{3}{2 \Delta t}, \quad (18)$$

$$f^{(n)} = \text{Pr}^{-1} \left[2(\mathbf{u} \cdot \nabla \omega)^{(n-1)} - (\mathbf{u} \cdot \nabla \omega)^{(n-2)} \right] - (2 \text{Pr} \Delta t)^{-1} \left(4\omega^{(n-1)} - \omega^{(n-2)} \right) - \text{Ra} \left(T_r \cos \theta - r^{-1} T_\theta \sin \theta \right)^{(n)}, \quad (19)$$

$$g^{(n)} = \left[2(\mathbf{u} \cdot \nabla T)^{(n-1)} - (\mathbf{u} \cdot \nabla T)^{(n-2)} \right] - (2 \Delta t)^{-1} \left(4T^{(n-1)} - T^{(n-2)} \right). \quad (20)$$

ABBD2 is an implicit-explicit (IMEX) method for solving the stiff advection-diffusion equations, where the diffusion is handled by the backward differentiation method and the advection terms are handled by the Adam-Bashforth method. Furthermore, explicit and nonlinear terms in $f^{(n)}$ and $g^{(n)}$ are computed pseudo-spectrally, with an anti-aliasing filter detailed in [50]. Through properly arranging the IMEX operator splitting, the overall accuracy of this method is second order in time. This well-tested method has been implemented in various convection problems [51–53], yielding accurate solutions for a wide range of parameters.

Equations (15) to (17) are Helmholtz and Poisson equations that can be solved by standard numerical methods. Considering that $r \in (r_0, 1/2)$ and θ is periodic, we discretize r variable with a Chebyshev series and θ variable with a truncated Fourier expansion. For more details of this Fourier-Chebyshev method, see [51, 53]. With given initial and boundary data, (16) can be solved first to obtain $T^{(n)}$, which is inserted in $f^{(n)}$ so (15) can be solved next. Finally, (17) is solved with the known $\omega^{(n)}$.

Typically, we use 1024 Fourier modes and 128 Chebyshev nodes in our simulation, which yields resolved and accurate solutions. We further set $\Delta t = 5 \times 10^{-4} \text{Ra}^{-1/2}$ to maintain time-stepping accuracy and stability, considering that the characteristic flow speed scales as $|\mathbf{u}| \sim \sqrt{\text{Ra}}$ (to be shown later).

The main difficulty of solving Eqs. (15) to (17) is from the boundary conditions,

$$\psi = \psi_r = 0, \quad T_r = 0 \quad \text{at } r = r_0, \quad (21)$$

$$\psi = -Q(t), \quad \psi_r = 0, \quad T = \frac{1 - \sin \theta}{2} \quad \text{at } r = \frac{1}{2}. \quad (22)$$

In these boundary conditions, we have both Neumann and Dirichlet data on ψ , but no boundary data on ω . This situation can be handled by the influence matrix method [51], which is a method to numerically map the Neumann data of ψ to the Dirichlet data of ω .

Due to the nonzero flow circulation, we also have to determine the flux $Q(t) = (2\pi)^{-1} \int_0^{2\pi} \int_{r_0}^{1/2} u(r, \theta, t) dr d\theta$ in the Dirichlet data of ψ . Denoting the θ average of f as $\widehat{f} = (2\pi)^{-1} \int_0^{2\pi} f d\theta$ and averaging the \mathbf{e}_θ component of Eq. (1), we have

$$\frac{\partial \widehat{u}}{\partial t} + \widehat{(u_r v)} + \frac{\widehat{(uv)}}{r} = \text{Pr Ra} \widehat{(T \cos \theta)} + \text{Pr} \left(\frac{\partial^2 \widehat{u}}{\partial r^2} + \frac{1}{r} \frac{\partial \widehat{u}}{\partial r} - \frac{\widehat{u}}{r^2} \right), \quad (23)$$

$$\widehat{u}(r_0, t) = \widehat{u}(0.5, t) = 0. \quad (24)$$

At time $t = n\Delta t$, values of $u^{(n-1)}$, $v^{(n-1)}$ are known and $T^{(n)}$ can be solved by Eq. (16) first, therefore we can solve $\widehat{u}(r, t)$ pseudo-spectrally with Chebyshev method. Finally, $Q(t) = \int_{r_0}^{1/2} \widehat{u}(r, t) dr$.

B. Numerical results

In this section, we briefly present some results of the DNS and show how tuning parameters like Ra can lead to diverse dynamical states. In all simulations, we set the inner radius to be $r_0 = 0.4$ so that dynamics are confined to a relatively narrow annulus. At $\text{Pr} = 4$, numerically solving Eqs. (1) to (7) yields fluid motions shown in Fig. 1, with corresponding movies included in the Supplemental Material. Figure 1(b) shows the low-Ra case, in which buoyancy is too weak to overcome viscous forces. In this conductive state, the fluid is motionless, and the only mechanism for thermal transport is conduction. As Ra increases, the destabilizing buoyancy becomes strong enough to drive a circulating flow shown in Fig. 1(c), where the fluid circulates unidirectionally in either the CW or CCW direction. At even higher Ra, Fig. 1(d) shows that the flow is no longer unidirectional, but reverses between CW and CCW in a chaotic manner. Counterintuitively, this reversal becomes regular as Ra gets even higher, where the flow is turbulent but the bulk motion reverses periodically as shown in Fig. 1(e).

To better capture the circulatory nature of flow in the thin channel, Fig. 2 shows the time series of the angular momentum $L(t)$ as defined in Eq. (11). At each Pr, the general trend of conductive, circulating, and reversal flow patterns emerges as

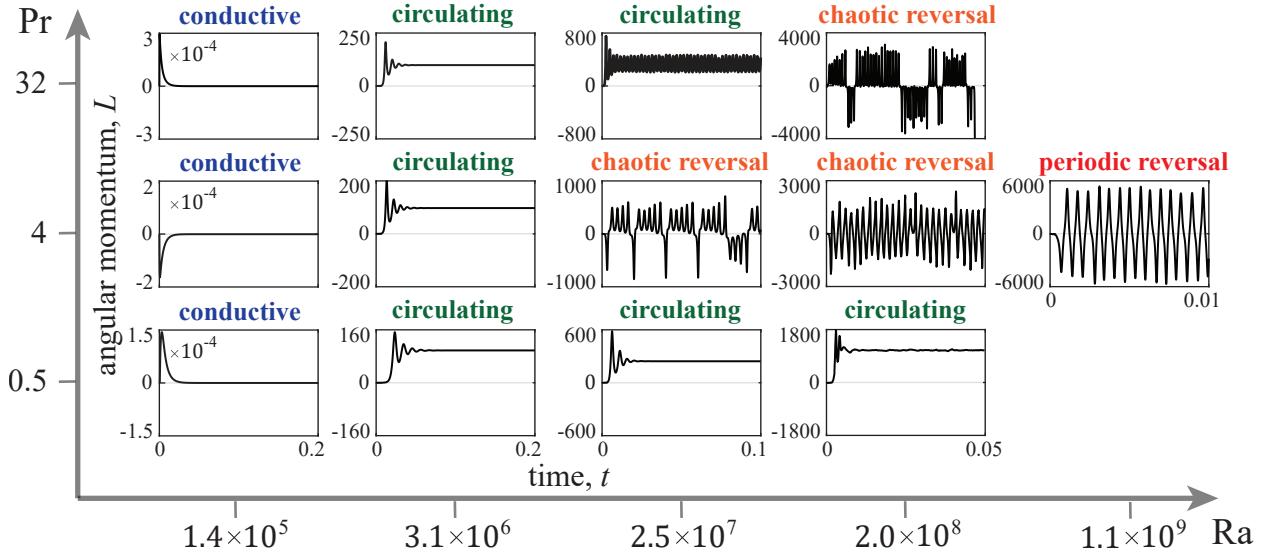


FIG. 2. Angular momentum L at various Ra and Pr reflecting the strength and direction of circulation. Four states of motion can be identified: conductive, circulating, chaotic reversal, and periodic reversal states. In all simulations, $r_0 = 0.4$.

we increase Ra , where the critical Ra separating these states differs depending on Pr . At $Ra = 1.4 \times 10^5$ (first column of Fig. 2), the motionless conductive state is a stable equilibrium for all the DNS presented, as initially added perturbation in L decays rapidly. In this case, a steady state exists for Eqs. (1) to (7) which has no flow ($L = 0$) and a conductive temperature profile given by Eq. (8).

The second column of Fig. 2 shows the case $Ra = 3.1 \times 10^6$, in which the flow reaches a steady circulating state with nonzero angular momentum. Although all the circulating states in Fig. 2 have a CCW direction, we note that CW circulating flow is also possible, depending on the initial distribution of temperature and flow.

So far, the flow and temperature profiles are steady as $t \rightarrow \infty$, however this steadiness is lost as we increase Ra to 2.5×10^7 for $Pr = 4$. This particular case shows that a steady circulating flow can also destabilize, leading to the state of chaotic reversal, where the circulation is no longer unidirectional and the flow switches between CW and CCW directions. The dynamics of $L(t)$ are chaotic, as small perturbations to the initial condition lead to very different trajectories. We will later show that the Lyapunov exponent in this case is large.

Although one might expect the state of chaos to persist, or even intensify, as the Rayleigh number increases, surprisingly order returns at sufficiently high Ra . At the Rayleigh number of 1.1×10^9 (last column of Fig. 2), the trajectory of $L(t)$ oscillates periodically, even though the flow structure is far from trivial as shown in the supplemental movies. How does this oscillatory state appear even though the flow is turbulent? What determines the frequency of the reversals? We address these questions in later sections through a simplified ODE model that links this periodic flow reversal to the oscillation of a mechanical pendulum.

The reversal states also exist for simulations with different Pr shown in Fig. 2, with an exception of those with $Pr = 0.5$ where the dynamics do not transition to chaos. Through investigation of the ODE model in later sections, we identify a critical Prandtl number Pr^* , below which the state of steady circulation remains stable for arbitrarily large Ra .

In Fig. 2, the scale of L apparently depends on Ra and Pr . As a measure of this scale, we define the root mean square of L as

$$L_{\text{rms}} = \sqrt{\langle L^2 \rangle}, \quad (25)$$

where $\langle \cdot \rangle$ is the time average operation. Figure 3(a) shows that L_{rms} remains zero for low Ra until a critical value $Ra_1^* = 7.25 \times 10^5$ (this value will be identified later), at which point L_{rms} grows positive with increasing Ra . That is, higher Ra results in stronger circulation. In the high Ra limit, $L_{\text{rms}} \propto \sqrt{Ra}$ and has a weak dependence on Pr .

The flow velocity on the other hand, can be represented by the Reynolds number,

$$Re = Pr^{-1} \langle \max |\mathbf{u}| \rangle, \quad (26)$$

where we use the maximum flow speed $\max |\mathbf{u}|$ to represent the velocity scale and Pr to represent the scale of kinematic viscosity. We note that the definition Eq. (26) is a consequence of our non-dimensionalization procedure, where we have rescaled the length by h and speed by κ/h , so $Re = h \langle |U| \rangle / \nu = (\kappa/\nu) \max |\mathbf{u}|$, where U is the maximum dimensional flow speed.

Shown in Fig. 3(b), Re also becomes nonzero as $Ra > Ra_1^*$, indicating the onset of fluid motion. At high Ra , Re also has a power-law dependence with Ra that has an exponent near 0.5, agreeing with the value obtained from Rayleigh-Bénard

convection [4, 53]. Interestingly, the scale of flow speed $\max|\mathbf{u}|$ at a constant Ra is not strongly influenced by Pr, as Re at a fixed Ra is inversely proportional to Pr in Fig. 3(b).

After analyzing the flow structures, we now turn our attention to the heat transfer. To measure the amount of heat passing through the fluid, we define the dimensionless Nusselt number,

$$\text{Nu} = \frac{\langle q \rangle}{\langle q_{\text{cond}} \rangle} = \frac{\langle \int_0^\pi (\partial_r T)|_{r=1/2} d\theta \rangle}{\langle \int_0^\pi (\partial_r T_{\text{cond}})|_{r=1/2} d\theta \rangle}. \quad (27)$$

Above, q is the total heat flux measured in the DNS, while q_{cond} is the heat flux associated with the conductive temperature field in Eq. (8). Naturally, $\text{Nu} = 1$ for solids and motionless fluids, while thermal convection gives $\text{Nu} > 1$, meaning the moving fluid is able to carry more heat convectively. Indeed, we observe this transition in Fig. 3(c), where a sudden increase of Nu can be spotted at Ra_1^* . In the limit of high Ra, a power law scaling $\text{Nu} \sim \text{Ra}^{0.27}$ emerges, similar to the scaling observed in the Rayleigh-Bénard convection (i.e. planar boundaries) [4, 17, 53].

With the simple geometry of an annulus, it becomes possible to analyze the flow and temperature dynamics of thermal convection. In the next section, we derive a low-dimensional dynamical system to reconcile the observations from DNS.

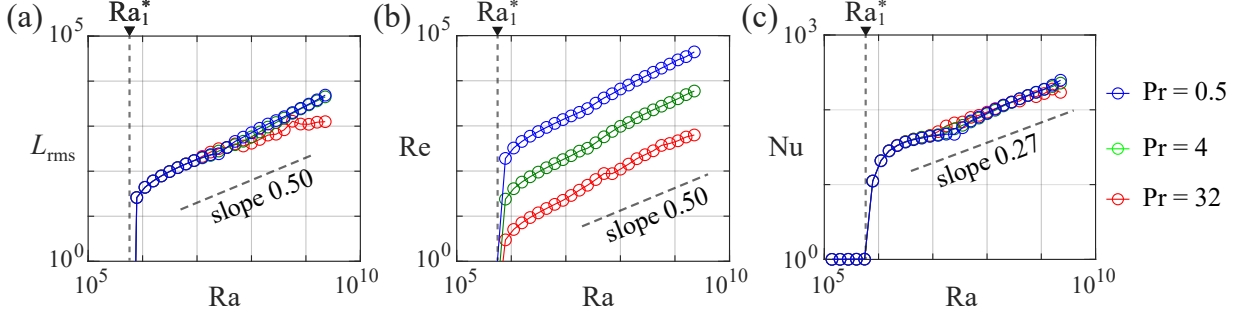


FIG. 3. Time-averaged bulk quantities of the flow and temperature fields. (a) RMS value of angular momentum L_{rms} represents the circulation strength. (b) Reynolds number Re indicates the scale of flow speed. (c) Nusselt number Nu measures the heat passing through the fluid domain. In all simulations, $r_0 = 0.4$, and a common critical Rayleigh number can be identified as $\text{Ra}_1^* = 7.25 \times 10^5$.

IV. LOW-DIMENSIONAL DYNAMICAL SYSTEM

In this section, we derive a low-dimensional ODE system for thermal convection in an annulus. Importantly, the system is cast in terms of physically relevant variables: the average angular momentum $L(t)$ and CoM coordinates $(X(t), Y(t))$ as defined in Eqs. (9) and (11) respectively. These variables permit a transparent description of the circulatory flow fields and buoyancy variations characterizing thermal convection.

The ODE system derives systematically from Galerkin truncation of the governing equations, a strategy that has been successfully employed for other systems [54–57]. In particular, we perform a Fourier-Laurent expansion of solutions to the NSB system and truncate to the lowest-order capable of satisfying all boundary conditions on the inner and outer rings of the annulus. The velocity field that results from this process is a shear flow in the angular direction, $u = u(r)$ and $v = 0$, which best approximates the true flow when the annulus is relatively narrow, i.e. $r_0 \approx 1/2$. For this reason, we set $r_0 = 0.4$ in the majority of numerical experiments. For smaller values of r_0 , we expect the ODE model to still capture the leading-order dynamics of the full system, but with larger quantitative differences.

A. Derivation of ODE system

When expressed in polar coordinates, the angular component of Eq. (1) and the incompressibility constraint Eq. (3) take the form

$$u_t + v u_r + \frac{1}{r} u u_\theta + \frac{1}{r} u v = -\frac{1}{r} p_\theta + \text{RaPr} T \cos \theta + \text{Pr} \left(u_{rr} + \frac{1}{r} u_r + \frac{1}{r^2} u_{\theta\theta} - \frac{1}{r^2} u + \frac{2}{r^2} v_\theta \right), \quad (28)$$

$$v_r + \frac{1}{r} v + \frac{1}{r} u_\theta = 0. \quad (29)$$

Multiplying Eq. (28) by r^2 , integrating over the annulus Ω , applying incompressibility Eq. (29) and the no-slip condition Eq. (5), and using the CoM definition Eq. (9) gives the evolution equation

$$\dot{L} = -\text{RaPr} X + \frac{\text{Pr}}{\text{A}_0} \int_0^{2\pi} (r^2 u_r) \Big|_{r_0}^{r_1} d\theta. \quad (30)$$

This equation is *exact* within the NSB framework. The first term, $-\text{Ra Pr } X$, represents torque due to an off-center CoM, much like in a pendulum system. This torque tends to destabilize the top-heavy conductive state. For example, if the CoM is perturbed to the left, $X < 0$, then $-\text{Ra Pr } X > 0$, which increases L . Since the conductive CoM is raised, $y_0 > 0$, increasing CCW angular momentum carries X farther left, creating the positive feedback associated with instability. The second term involving $(r^2 u_r)|_{r_0}^{r_1}$ acts as damping. For example, if the rotation is primarily CCW with $L > 0$, then $u > 0$ on average. Thus, in order to satisfy the no-slip boundary conditions, u must decrease as r approaches the inner or outer boundary, $r \rightarrow r_0^+$ or $r \rightarrow 1/2^-$ respectively, both giving $(r^2 u_r)|_{r_0}^{r_1} < 0$ and thus reducing the angular momentum.

We next introduce some approximations to supplement the exact evolution Eq. (30) and obtain a closed system for the variables $L(t), X(t), Y(t)$. Since the temperature distribution $T(r, \theta, t)$ is periodic in θ , it can be written as a Fourier series with no approximation made,

$$T(r, \theta, t) = a_0(r, t) + \sum_{n=1}^{\infty} a_n(r, t) \cos n\theta + b_n(r, t) \sin n\theta, \quad (31)$$

From (6)–(7), the coefficients inherit boundary conditions

$$\partial_r a_n = \partial_r b_n = 0 \quad \text{at } r = r_0, \quad (32)$$

$$a_0 = 1/2, b_1 = -1/2, \text{ all others vanish at } r = 1/2. \quad (33)$$

Similarly, both velocity components are periodic in θ , and so each can be written as a (complex) Fourier series

$$u(r, \theta, t) = \sum_{n=-\infty}^{\infty} \hat{u}_n(r, t) e^{in\theta}, \quad v(r, \theta, t) = \sum_{n=-\infty}^{\infty} \hat{v}_n(r, t) e^{in\theta}. \quad (34)$$

The no-slip boundary conditions, Eq. (5), and incompressibility, Eq. (29), respectively yield the conditions

$$\hat{u}_n(r, t) = \hat{v}_n(r, t) = 0 \quad \text{at } r = r_0 \text{ and } r = 1/2, \quad (35)$$

$$in\hat{u}_n + \hat{v}_n + r\partial_r \hat{v}_n = 0 \quad (36)$$

holding for each n .

We now aim to truncate the Fourier expansions, Eqs. (31) and (34), *to the lowest order capable of satisfying all boundary conditions*. In particular, we retain up to the $n = 1$ mode in the temperature field and the $n = 0$ in the velocity field. It is necessary to retain the $n = 1$ mode in the temperature field to satisfy the thermal condition, Eq. (33), whereas only the $n = 0$ mode in the flow field is needed to satisfy the no-slip conditions, Eq. (35). Enforcing incompressibility, Eq. (36), implies that $\hat{v}_0(r, t) = 0$, which shows that the leading-order flow structure is shear $(u, v) \sim (\hat{u}_0(r, t), 0)$.

The thermal transport equation, Eq. (2), written in polar coordinates is

$$T_t + \frac{u}{r} T_\theta + v T_r = \frac{1}{r} \frac{\partial}{\partial r} (r T_r) + \frac{1}{r^2} T_{\theta\theta}. \quad (37)$$

Inserting the Fourier expansion Eq. (31) and the truncated velocity fields, $(u, v) = (\hat{u}_0(r, t), 0)$, into Eq. (37), multiplying by r^2 , and projecting onto Fourier mode n gives

$$r^2 \dot{a}_n = -nr \hat{u}_0(r, t) b_n - n^2 a_n + r \partial_r (r \partial_r a_n), \quad (38)$$

$$r^2 \dot{b}_n = +nr \hat{u}_0(r, t) a_n - n^2 b_n + r \partial_r (r \partial_r b_n). \quad (39)$$

At order $n = 0$, the above gives a diffusion equation for $a_0(r, t)$,

$$\dot{a}_0 = r^{-1} \partial_r (r \partial_r a_0). \quad (40)$$

Boundary conditions (32)–(33) imply $\lim_{t \rightarrow \infty} a_0(r, t) = 1/2$, regardless of initial conditions. We will therefore set $a_0 = 1/2$ henceforth, as variations from this value simply represent transient dynamics that are decoupled from the rest of the system.

From Eq. (9), the CoM coordinates are given by

$$X(t) = -\frac{\pi}{A_0} \int_{r_0}^{1/2} r^2 a_1(r, t) dr, \quad Y(t) = -\frac{\pi}{A_0} \int_{r_0}^{1/2} r^2 b_1(r, t) dr. \quad (41)$$

Differentiating with respect to time, inserting Eqs. (38) and (39) with $n = 1$, and simplifying yields the formulas

$$\dot{X} = \frac{\pi}{A_0} \int_{r_0}^{1/2} r \hat{u}_0(r, t) b_1(r, t) dr - \frac{\pi}{A_0} \left(r^2 \frac{\partial a_1}{\partial r} - r a_1 \right) \Big|_{r_0}^{r_1}, \quad (42)$$

$$\dot{Y} = -\frac{\pi}{A_0} \int_{r_0}^{1/2} r \hat{u}_0(r, t) a_1(r, t) dr - \frac{\pi}{A_0} \left(r^2 \frac{\partial b_1}{\partial r} - r b_1 \right) \Big|_{r_0}^{r_1}. \quad (43)$$

We now assume special forms for the radial dependence of the variables $a_1(r, t)$, $b_1(r, t)$, and $\hat{u}_0(r, t)$. Guided by the conductive-state solution, (8), we assume truncated Laurent expansions for the coefficients a_1 and b_1 :

$$a_1(r, t) = \frac{1}{2}A(t)(2r - 1)(1 - 2r_0^2r^{-1}), \quad (44)$$

$$b_1(r, t) = -\frac{1}{2} + \frac{1}{2}B(t)(2r - 1)(1 - 2r_0^2r^{-1}). \quad (45)$$

These are the most general Laurent expansions containing powers r^{-1} , r^0 , r^1 and satisfying boundary conditions Eqs. (32) and (33). Setting $A(t) = 0$, $B(t) = -(4r_0^2 + 1)^{-1}$ recovers the conductive-state solution, Eq. (8), exactly, whereas allowing these coefficients to vary creates different buoyancy fields.

Also guided by the Laurent expansion, we assume the following form for the angular velocity

$$\hat{u}_0(r, t) = C(t)(r - r_0)(1 - 2r)r^{-1}. \quad (46)$$

Similarly, this is the most general Laurent expansion that contains powers r^{-1} , r^0 , r^1 and that satisfies the no-slip conditions Eq. (35). Setting $C(t) = 0$ trivially recovers the conductive state, whereas allowing this coefficient to vary creates different circulatory flow fields.

Inserting Eqs. (44) and (45) into Eq. (41) and integrating yields the following linear relationships between the CoM coordinates and the coefficients $A(t)$, $B(t)$:

$$X(t) = \left(\frac{(1 - 2r_0)^2(1 + 6r_0 + 16r_0^2)}{48(1 + 2r_0)} \right) A(t), \quad (47)$$

$$Y(t) = \frac{1 + 2r_0 + 4r_0^2}{12(1 + 2r_0)} + \left(\frac{(1 - 2r_0)^2(1 + 6r_0 + 16r_0^2)}{48(1 + 2r_0)} \right) B(t). \quad (48)$$

Meanwhile, from Eq. (46) and the definition of angular momentum, Eq. (11), $L(t)$ relates linearly to $C(t)$ through

$$L(t) = \frac{2\pi}{A_0} \int_{r_0}^{1/2} r^2 u(r, t) dr = \frac{(1 - 2r_0)^2}{12} C(t). \quad (49)$$

Inserting Eq. (46) into Eq. (30), using the linear relationship Eq. (49), and simplifying gives the evolution equation

$$\dot{L} = -\text{RaPr} X - \alpha \text{Pr} L, \quad (50)$$

where $\alpha = 48/(1 - 2r_0)^2$. Meanwhile, inserting Eqs. (44)–(49) into Eqs. (42) and (43), performing exact integration and simplifying gives the following evolution equations for the CoM coordinates:

$$\dot{X} = -kLY + \gamma L - \beta X, \quad (51)$$

$$\dot{Y} = +kLX + \delta - \beta Y. \quad (52)$$

Here, the coefficients α , β , δ , k , and γ are each functions of r_0 only, as given by:

$$\alpha = \frac{48}{(1 - 2r_0)^2}, \quad \beta = \frac{48(1 + 4r_0^2)}{(1 - 2r_0)^2(1 + 6r_0 + 16r_0^2)}, \quad \delta = \frac{3(1 + 12r_0^2)}{(1 - 2r_0)^2(1 + 6r_0 + 16r_0^2)}, \quad (53)$$

$$k = 24 \frac{(1 - 2r_0)(1 - 6r_0 - 4r_0^2 - 88r_0^3 + 32r_0^4) - 96r_0^3 \ln(2r_0)}{(1 - 2r_0)^5(1 + 6r_0 + 16r_0^2)}, \quad (54)$$

$$\gamma = \frac{(1 - 4r_0^2)(1 - 8r_0 - 224r_0^3 - 80r_0^4) - 192r_0^3(1 + 2r_0 + 4r_0^2) \ln(2r_0)}{(1 - 2r_0)^5(1 + 2r_0)(1 + 6r_0 + 16r_0^2)}. \quad (55)$$

Two important length scales naturally arise from grouping like terms in Eqs. (51) and (52):

$$y_0 = \delta/\beta \quad \text{The height of the conductive-state CoM,} \quad (56)$$

$$y_1 = \gamma/k \quad \text{The height of the pendulum fulcrum,} \quad (57)$$

where the interpretations will be justified momentarily. With these definitions, the self-contained dynamical system Eqs. (50) to (52) becomes

$$\dot{L} = -\text{RaPr} X - \alpha \text{Pr} L, \quad (58)$$

$$\dot{X} = -kL(Y - y_1) - \beta X, \quad (59)$$

$$\dot{Y} = +kLX - \beta(Y - y_0). \quad (60)$$

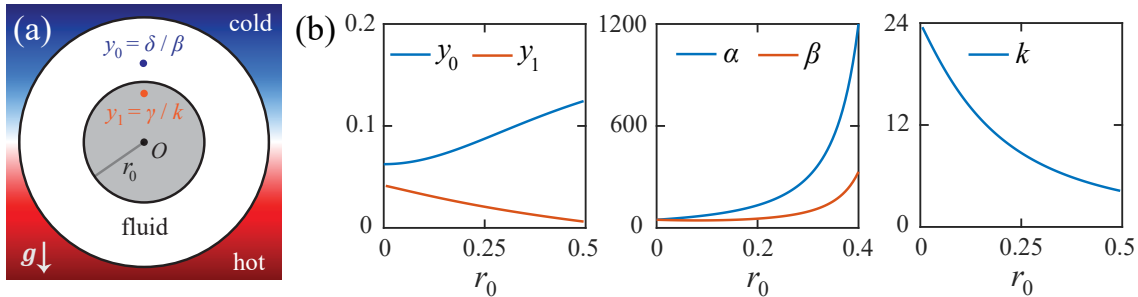


FIG. 4. Pendulum structure of the ODE system. (a) Equations (58) to (60) correspond to a pendulum with fulcrum y_1 and forcing term that drives the CoM towards y_0 . (b) The constants in the ODE model depend on r_0 only; y_0 always lies above the fulcrum, y_1 , implying that $\Delta y = y_0 - y_1 > 0$ for any r_0 .

The above form offers some important physical insight. First, if there is no flow $L = 0$, Eqs. (59) and (60) show that the CoM converges to the point $(X, Y) = (0, y_0)$ with y_0 given by Eq. (56). At the same time, no fluid motion produces the conductive-state solution Eq. (8), with CoM height given by Eq. (10). Hence, Eq. (56) must correspond to Eq. (10), and this can be verified directly; both give equivalent formulas for the height of the conductive-state CoM.

Second, if $\beta = 0$, Eqs. (58) to (60) are *mathematically identical* to those of a damped pendulum with angle $\phi(t)$, mass m , and length l . Equations (58) to (60) are simply written in terms of the bob's Cartesian coordinates $(X, Y) = (l \sin \phi, y_1 - l \cos \phi)$ and angular momentum $L = ml^2 \dot{\phi}$. In this analogy, the gravitational constant is $g = kl^2 \text{RaPr}$, and the damping coefficient is αPr . Most importantly, Eq. (59) shows that fulcrum of the pendulum lies at the point $(0, y_1)$ with y_1 given by Eq. (57).

The terms in Eqs. (59) and (60) with prefactor β arise from the interaction of boundary heating and thermal diffusion. These terms drive the CoM towards the conductive-state CoM $(0, y_0)$. Through Eqs. (56) and (57), it can be shown that $0 < y_1 < y_0$ for any r_0 , implying that these terms act to raise the CoM above the fulcrum and, hence, tend to destabilize the system. Figure 4(a) illustrates these two heights, y_0 and y_1 , and Fig. 4(b) shows their dependence on r_0 . A crucial parameter that appears in the stability analysis is the distance $\Delta y = y_0 - y_1 > 0$, which is positive for any r_0 as seen in Fig. 4(b). Also seen in Fig. 4(b) is the dependence of the parameters α, β , and k on r_0 .

It is important to remember that the constants in the ODE model, α, β, k, y_0 , and y_1 , are purely geometric in that they depend on r_0 only as given by Eqs. (53) to (55). The only parameters that depend on other physical properties, such as the strength of thermal forcing, the viscosity, etc., are Ra and Pr .

B. Simulation of ODE system in comparison to DNS

In this section, we discuss numerical solutions of the ODE system, Eqs. (58) to (60), in comparison to the fully-resolved DNS of Eqs. (1) to (7). Numerical solutions of the ODE system are found with MATLAB's *ode45*. As in previous sections, we fix $\text{Pr} = 4$ and $r_0 = 0.4$, and vary the Rayleigh number. Figure 5 shows solution trajectories of $(L(t), X(t), Y(t))$ computed from both the DNS (top panel) and the ODE system (bottom panel) for a sequence of four Rayleigh numbers. In each case, we prescribe the same initial conditions in the DNS and ODE system. The resulting solution trajectories are remarkable similar in all four cases, and in fact nearly identical in the first two [Fig. 5(a)–(b)], suggesting that the simplified ODE system recovers detailed convective dynamics across a range of Rayleigh numbers.

The first two cases [Fig. 5(a)–(b)] feature the lowest Rayleigh numbers, $\text{Ra} = 7.8 \times 10^5$ and 3.1×10^6 respectively. In each case, the solution $(L(t), X(t), Y(t))$ converges to a fixed point with non-zero angular momentum, $L \neq 0$, and a CoM that is raised, $Y > 0$, and off-set, $X \neq 0$. This type of fixed point corresponds to the steadily circulating state seen in Fig. 1(c); the fluid rotates in either the CW or CCW direction at constant rate. The cases shown in Fig. 5(a)–(b) exhibit CCW rotation $L > 0$ as a result of the initialization. The main difference between Fig. 5(a) and Fig. 5(b), is that at $\text{Ra} = 7.8 \times 10^5$ the system converges to the circulating state as an overdamped oscillator, and at higher Rayleigh, $\text{Ra} = 3.1 \times 10^6$, the system converges as an underdamped oscillator.

At $\text{Ra} = 2.5 \times 10^7$, Fig. 5(c) shows more complex solution trajectories that appear to fill a higher-dimensional set. Measurements in Section V of this set's fractal dimension yield a value of 1.4, characteristic of a strange attractor. Each sign change of L seen in Fig. 5(c) indicates a reversal of the LSC. The view of the $L(t)$ time-series from Fig. 2 shows these reversals to occur erratically, suggesting chaotic dynamics. While it is difficult to directly compare two chaotic time series, the attracting sets obtained from DNS and from the ODE system appear remarkably similar, suggesting that the reduced ODE model captures the main features of convective dynamics in this regime.

Figure 5(d) shows the highest Rayleigh number, $\text{Ra} = 1.1 \times 10^9$. In this case, the ODE dynamics converge to a stable limit cycle, seen as the simple, closed curve in the bottom panel (the early-time convergence to the limit cycle is not shown). Since L changes sign, this limit cycle corresponds to periodic reversals of the LSC, much like was observed in the DNS

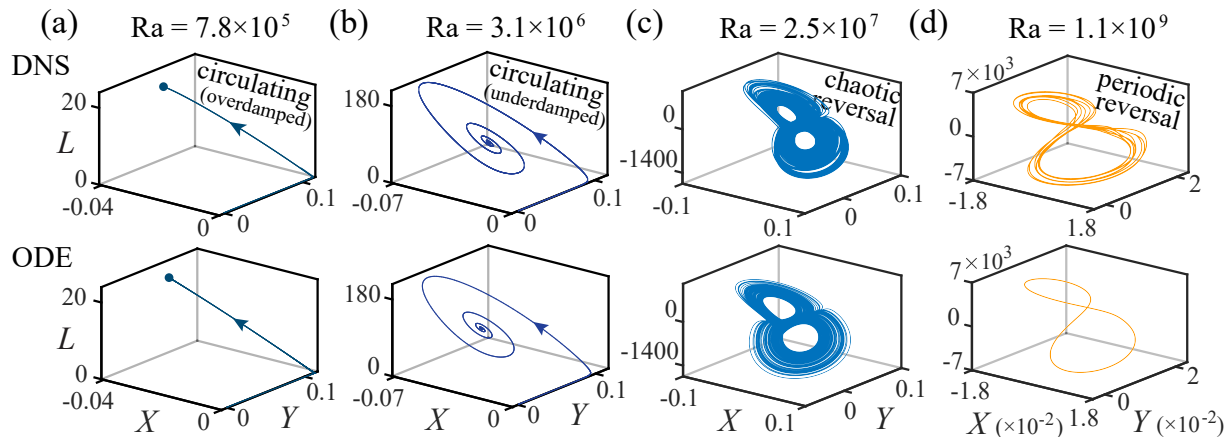


FIG. 5. Comparison between ODE model Eqs. (58) to (60) and fully-resolved DNS. (a) At $Ra = 7.8 \times 10^5$, the dynamical system is overdamped and the solution trajectory (L, X, Y) quickly approaches the steady circulating state. (b) At $Ra = 3.1 \times 10^6$, the dynamical system becomes underdamped and the solution is an inward spiral towards the steady circulating state. (d) Increasing Ra to 2.5×10^7 brings the trajectory to chaos, whose shape indicates a strange attractor with fractal dimension of 1.4. (e) Limit cycle appears at $Ra = 1.1 \times 10^9$, indicating a periodic solution. In all simulations, $Pr = 4$ and $r_0 = 0.4$. Movies of (b)-(d) are included in the Supplemental Material.

at high Ra (see the right-most panel of Fig. 2). The top panel of Fig. 5(d) shows that the DNS dynamics approximately follow a similarly shaped limit cycle, though with fluctuations about the cycle. In the DNS, the LSC reversals are nearly periodic, but with a small amount of variability. This variability will be quantified further in Section VI by measurements of the frequency spectrum. Despite the presence of fluctuations, the main shape of the limit cycle from DNS and the ODE model in Fig. 5(d) appear similar, again suggesting that the ODE model captures the leading-order convective dynamics well.

The close match between the ODE model and DNS observed in Fig. 5 suggests that the ODE model successfully captures the main features of convective dynamics across a range of Rayleigh numbers. Since the ODE model is substantially simpler, it may offer insight into the transitions between the different convective steps, and this idea is explored in the next section.

V. STABILITY AND BIFURCATION ANALYSIS

To better understand the transitions between different convective states, we now examine the stability and bifurcations of the ODE model, Eqs. (58) to (60). First, to locate the fixed points, we set $\dot{L} = 0$ and $\dot{Y} = 0$ to obtain

$$X = -\frac{\alpha}{Ra}L, \quad Y = y_0 - \frac{k\alpha}{\beta Ra}L^2. \quad (61)$$

Then setting $\dot{X} = 0$ yields a condition for the fixed points in terms of L only,

$$L [k^2\alpha L^2 - (\beta k Ra \Delta y - \alpha\beta^2)] = 0. \quad (62)$$

There can be up to three roots of this cubic equation:

$$L = 0, \quad L = \pm L_1 = \pm \frac{\beta}{k} \sqrt{\frac{k Ra}{\alpha\beta} \Delta y - 1}. \quad (63)$$

The first root, $L = 0$, corresponds to the conductive state. The second two roots, $L = \pm L_1$, are real only if the term under the radical is positive. These roots correspond to circulating states of constant angular momentum in either the CCW or CW direction ($+L_1$ and $-L_1$ respectively). The three roots yield three possible fixed points of the system:

$$L = 0, \quad X = 0, \quad Y = y_0 \quad \text{The conductive state,} \quad (64)$$

$$L = \pm L_1, \quad X = \mp \frac{\alpha}{Ra}L_1, \quad Y = y_1 + \frac{\alpha\beta}{kRa} \quad \text{The circulating states.} \quad (65)$$

For general (L, X, Y) , the Jacobian of Eqs. (58) to (60) is given by

$$J(L, X, Y) = \begin{bmatrix} -\alpha Pr & -Ra Pr & 0 \\ -k(Y - y_1) & -\beta & -kL \\ kX & kL & -\beta \end{bmatrix}. \quad (66)$$

Evaluating the Jacobian determines the type and stability of each fixed point.

A. $\text{Ra} < \text{Ra}_1^*$, stable conductive state

We now analyze bifurcations with respect to increasing Rayleigh number, Ra , while holding r_0 and Pr fixed. In particular, for Rayleigh numbers below the critical value,

$$\text{Ra}_1^* = \frac{\alpha\beta}{k\Delta y}, \quad (67)$$

the term under the radical in Eq. (63) is negative and so the circulating-state fixed points do not exist. Thus, for $\text{Ra} < \text{Ra}_1^*$ the conductive state, Eq. (64), is the only fixed point of the system. Evaluating the Jacobian gives

$$J_{\text{cond}} = \begin{bmatrix} -\alpha \text{Pr} & -\text{Ra} \text{Pr} & 0 \\ -k\Delta y & -\beta & 0 \\ 0 & 0 & -\beta \end{bmatrix}. \quad (68)$$

Consider the three eigenvalues z_1, z_2, z_3 of this matrix. Due to the zeros in the last row and last column, one eigenvalue is $z_1 = -\beta$. The other two are eigenvalues of the smaller 2×2 subsystem that excludes the final row and final column. The trace of this subsystem is negative, and the determinant is equal to $\text{Pr}(\alpha\beta - k\text{Ra}\Delta y)$, which transitions from positive to negative precisely as Ra crosses the threshold Ra_1^* . Thus, for $\text{Ra} < \text{Ra}_1^*$, all three eigenvalues are negative and so the conductive state corresponds to a stable node. For $\text{Ra} > \text{Ra}_1^*$, two eigenvalues are negative and one is positive, meaning the conductive state is a saddle point.

B. $\text{Ra}_1^* \leq \text{Ra} < \text{Ra}_2^*$, bistable circulating states

As Ra crosses the critical value Ra_1^* , the two circulating-state fixed points emerge, and, simultaneously, the conductive state loses stability. That is, a supercritical pitchfork bifurcation occurs. Evaluating the Jacobian at the circulating fixed points will show that they emerge as stable fixed points and then undergo stability transitions at yet higher Rayleigh numbers.

In particular, the Jacobian matrix, Eq. (66), evaluated at each circulating fixed-point, Eq. (65), is given by

$$J_{\pm} = \begin{bmatrix} -\alpha \text{Pr} & -\text{Ra} \text{Pr} & 0 \\ -\alpha\beta/\text{Ra} & -\beta & \mp kL_1 \\ \mp \alpha kL_1/\text{Ra} & \pm kL_1 & -\beta \end{bmatrix}. \quad (69)$$

The characteristic polynomial of this matrix is

$$P(z) = z^3 + c_2 z^2 + c_1 z + c_0, \quad (70)$$

$$c_0 = 2\alpha k^2 L_1^2 \text{Pr}, \quad (71)$$

$$c_1 = k^2 L_1^2 + \beta^2 + \alpha\beta \text{Pr}, \quad (72)$$

$$c_2 = \alpha \text{Pr} + 2\beta. \quad (73)$$

This cubic polynomial has three roots, z_1, z_2 , and z_3 . At least one root is guaranteed to be real, while the other two may either be real or form a complex-conjugate pair. The discriminant Δ determines which occurs,

$$\Delta = (z_1 - z_2)^2 (z_2 - z_3)^2 (z_1 - z_3)^2 = c_1^2 c_2^2 - 4c_0 c_2^3 + 18c_0 c_1 c_2 - 4c_1^3 - 27c_0^2. \quad (74)$$

If $\Delta \geq 0$, then all three roots are real, whereas if $\Delta < 0$, then two of the roots are complex conjugates.

We first consider Ra slightly above the critical value Ra_1^* , in which case $L_1^2 = O(\text{Ra} - \text{Ra}_1^*)$ is small. Substituting into (74) gives

$$\Delta = c_1^2 \alpha^2 \text{Pr}^2 + O(\text{Ra} - \text{Ra}_1^*). \quad (75)$$

Thus, if $\text{Ra} > \text{Ra}_1^*$ and Ra is sufficiently close to Ra_1^* , then $\Delta > 0$ and so all three roots are real. Furthermore, the coefficients c_0, c_1, c_2 are all positive, and so there cannot be any positive roots of Eq. (70). Therefore, in this case of Ra slightly above Ra_1^* , all three eigenvalues are negative, and so the circulating states correspond to bistable nodes.

As Ra continues to increase, the discriminant eventually becomes negative implying that two eigenvalues become complex. The precise Rayleigh number at which this occurs, denoted $\text{Ra}_{3/2}^*$, can be determined by setting $\Delta = 0$ in (74). As Ra crosses $\text{Ra}_{3/2}^*$, the circulating states transition from stable nodes to stable spirals. In the former stage, the system

behaves as an overdamped oscillator as seen in Fig. 5(a), and in the later stage, as an underdamped oscillator as seen in Fig. 5(b).

As Ra increases further beyond $Ra_{3/2}^*$, the circulating states eventually lose stability. To determine where the transition occurs, we use Vieta's formulas

$$z_1 + z_2 + z_3 = -c_2, \quad (76)$$

$$z_1 z_2 + z_2 z_3 + z_1 z_3 = c_1, \quad (77)$$

$$z_1 z_2 z_3 = -c_0. \quad (78)$$

where z_1, z_2, z_3 are the three eigenvalues, and c_0, c_1, c_2 are the coefficients given by Eqs. (71) to (73). Let z_1 denote the real eigenvalue and $z_{2,3} = \sigma \pm i\omega$ the complex-conjugate pair. Then the circulating-state fixed points are stable spirals if $\sigma < 0$ and unstable spirals if $\sigma > 0$. The transition occurs at $\sigma = 0$, which implies that $z_2 + z_3 = 0$ and $z_2 z_3 = \omega^2$. Inserting into Eqs. (76) to (78) gives $z_1 = -c_2$, $\omega^2 = c_1$, and $z_1 \omega^2 = -c_0$ respectively, which combine to give $c_0 = c_1 c_2$. Substituting this relationship into the definition of the coefficients, Eqs. (71) to (73), yields

$$2\alpha k^2 L_1^2 Pr = (k^2 L_1^2 + \beta^2 + \alpha\beta Pr)(\alpha Pr + 2\beta), \quad (79)$$

Recall that the Rayleigh number appears in $k^2 L_1^2$ through

$$k^2 L_1^2 = \alpha^{-1} \beta k Ra \Delta y - \beta^2. \quad (80)$$

Therefore, solving (79) for $k^2 L_1^2$ yields the critical Rayleigh number Ra_2^* at which the circulating states lose stability,

$$Ra_2^* = \frac{\alpha^2 Pr}{k \Delta y} \left(\frac{\alpha Pr + 4\beta}{\alpha Pr - 2\beta} \right). \quad (81)$$

Beyond this threshold, all fixed points of the system are unstable.

C. $Ra \geq Ra_2^*$, chaos and eventual return to order

As Ra crosses Ra_2^* , a Hopf bifurcation occurs and the circulating states change from stable to unstable spiral points. Past this critical value, all fixed points of the system are unstable, thereby introducing the possibility of chaotic dynamics as supported by the numerical observations in Fig. 5(c). Before analyzing the chaotic state, the explicit form of Eq. (81) offers a few simple observations. First, for Pr smaller than the critical value

$$Pr^* = 2\beta/\alpha, \quad (82)$$

the denominator in Eq. (81) is negative, implying that there is no Ra_2^* threshold. That is, if $Pr \leq Pr^*$ and the circulating states exist, then they remain stable no matter how large the Rayleigh number is. Thus, $Pr \leq Pr^*$ precludes the possibility of chaos; trajectories are simply attracted to one of the bistable circulating states or to the conductive state.

The second observation is that taking the limit $Pr \rightarrow \infty$ in Eq. (81) shows that the threshold Ra_2^* scales linearly with Pr with prefactor $\alpha^2/(k\Delta y)$. That is, large Pr numbers require large Ra values to reach the chaotic regime. Since large Ra values generally require greater computational expense in DNS, this observation suggests that the most practical way to realize the chaotic state in the DNS is to choose Pr above the threshold Eq. (82), but not too large.

The value $r_0 = 0.4$ chosen for Fig. 5 gives $\alpha = 1200, \beta = 330, k = 5.5, \Delta y = 0.1, Pr^* = 0.55$, and $Ra_1^* = 7.3 \times 10^5$. These values, combined with the choice $Pr = 4$, yields $Ra_2^* = 1.6 \times 10^7$. Thus, the values of $Ra = 7.8 \times 10^5$ and $Ra = 3.1 \times 10^6$ used in Fig. 5(a)–(b) lie in the range $[Ra_1^*, Ra_2^*]$, for which stability analysis predicts the circulating states to be stable fixed points. This prediction is confirmed by both the DNS and ODE numerical trajectories shown in the figure. Meanwhile, the value $Ra = 2.5 \times 10^7$ used in Fig. 5(c) lies above the Ra_2^* threshold for which the analysis predicts all fixed points to be unstable. Again, this prediction is consistent with the chaotic numerical trajectories observed in the figure. Lastly, the value $Ra = 1.1 \times 10^9$ also exceeds the Ra_2^* threshold, but rather than chaotic dynamics, trajectories converge towards a stable limit cycle. In summary, all of the numerical trajectories from both DNS and the ODE system shown in Fig. 5 are consistent with the threshold values, Eqs. (67) and (81), predicted by stability analysis.

An important insight provided by the numerical trajectories in Fig. 5(c)–(d) is that, for $Ra \geq Ra_2^*$, the long-time dynamics may either be chaotic, as in Fig. 5(c), or periodic, as in Fig. 5(d); both behaviors are consistent with the conclusion from stability analysis that all fixed points are unstable. Figure 5, however, only shows a selection of four particular Rayleigh numbers, and thus offers only a coarse evaluation of the predictions from stability analysis. In the next section, we conduct a more thorough comparison.

D. Stability results in comparison to numerical trajectories

In this section, we systematically compare the predictions of the stability analysis with the numerical trajectories of Eqs. (58) to (60). In particular, we examine bifurcations with respect to increasing Rayleigh number. Figure 6 shows long-time numerical trajectories of the CoM coordinates, $(X(t), Y(t))$, plotted against Ra on the horizontal axis ($L(t)$ is not shown). The Prandtl number is set to $Pr = 4$ and 0.25 in Fig. 6(a) and (b) respectively.

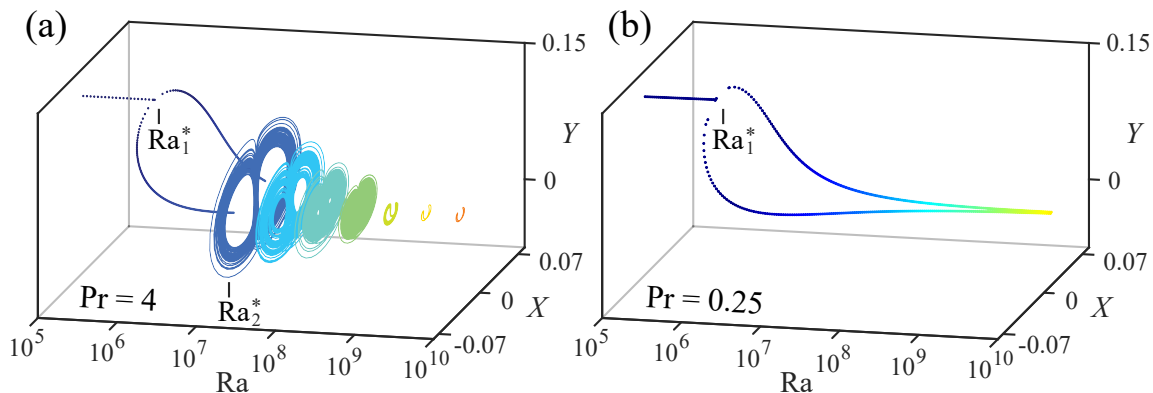


FIG. 6. Bifurcation diagrams show long-time trajectories of CoM coordinates, (X, Y) , computed numerically from the ODE system Eqs. (58) to (60). Trajectories are plotted against Rayleigh number, with $r_0 = 0.4$ and with $Pr = 4$ and 0.25 in (a) and (b) respectively. In both cases, a pitchfork bifurcation occurs at Ra_1^* predicted by Eq. (67), where the bistable circulating states emerge as stable nodes. (a) For $Pr = 4$, a second, Hopf bifurcation occurs at Ra_2^* predicted by Eq. (81), where the circulating states lose stability and chaotic dynamics emerge. For $Ra > 10^9$, chaos gives way to periodic dynamics. (b) For $Pr = 0.25$, below the threshold value $Pr^* = 0.55$ from Eq. (82), the circulating states remain stable for arbitrarily large Ra .

For low Ra , both figures show that long-time dynamics collapse to a single stable fixed point that corresponds to the conducting state. As Ra increases, a supercritical pitchfork bifurcation occurs precisely at the value $Ra = Ra_1^*$ predicted by Eq. (67). This value, $Ra_1^* = 7.3 \times 10^5$, is independent of Pr , and thus the pitchfork bifurcation occurs at exactly the same location in both (a) and (b). The two branches to the right of the pitchfork represent the bistable circulating states.

As Ra increases further, Fig. 6(a) shows that a Hopf bifurcation occurs at the value $Ra = Ra_2^* = 1.6 \times 10^7$ predicted by Eq. (81). Here, the circulating states lose stability and give way to chaotic dynamics, seen by the blue, turquoise, teal, and green trajectories. Meanwhile, Fig. 6(b) does not exhibit a Hopf bifurcation. In Fig. 6(b), the Prandtl number 0.25 lies below the critical value $Pr^* = 0.55$ predicted by Eq. (82). Therefore, the bistable circulating states remain stable for arbitrarily large Ra , as is consistent with the trajectories seen in Fig. 6(b).

Returning to Fig. 6(a), as Ra increases further beyond Ra_2^* , the chaotic dynamics eventually subside and give way to the more confined and regular dynamics, shown by the green, yellow, and red trajectories. The figure suggests the transition to occur at roughly $Ra = 10^9$. These trajectories resemble small circular arcs, consistent with pendulum motion. Furthermore, Fig. 5(d) shows that the corresponding dynamics are periodic, or in the case of DNS, nearly periodic.

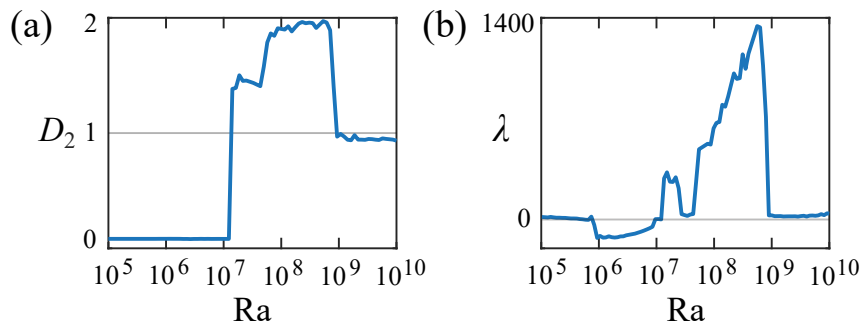


FIG. 7. The fractal dimension D_2 and Lyapunov exponent λ from trajectories in Fig. 6(a) characterize states of order and chaos. (a) For $Ra < Ra_2^*$, the fractal dimension is nearly zero, reflecting convergence to a fixed point. As Ra crosses Ra_2^* , the fractal dimension abruptly increases to a value in the range $1 < D_2 < 2$, characteristic of a strange attractor. For $Ra > 10^9$, D_2 drops back to unity, reflecting convergence to a one-dimensional limit cycle. (b) For $Ra < Ra_2^*$, the Lyapunov exponent is nearly zero or negative, consistent with convergence to a fixed point. As Ra crosses Ra_2^* , λ suddenly grows large, indicating extreme sensitivity to initial conditions that is characteristic of chaotic dynamics. For $Ra > 10^9$, λ is nearly zero, reflecting a return to order.

To further quantify the chaotic regime and distinguish it from the orderly dynamics, Fig. 7 shows the fractal dimension D_2 (specifically the correlation dimension [58]) and the Lyapunov exponent λ corresponding to the trajectories shown in

Fig. 6(a). The figure shows that at low Ra, the fractal dimension is zero and the Lyapunov exponent is small or negative, consistent with convergence to a stable fixed point (either the conducting state or one of the circulating states). As Ra crosses $Ra_2^* = 1.6 \times 10^7$, D_2 suddenly increases beyond unity and λ grows large. For Ra in the range $[Ra_2^*, 10^9]$, the value of D_2 indicates a strange attractor with dimension in between 1 and 2, while the large value of λ indicates extreme sensitivity to initial conditions. Both observations suggest chaotic dynamics. As Ra crosses 10^9 , D_2 suddenly drops to approximately one and λ drops to nearly zero, indicating a return to orderly dynamics, specifically periodic motion along a one-dimensional limit cycle.

VI. RETURN TO ORDER AT HIGH RAYLEIGH NUMBER

Figures 5 to 7 demonstrate that at very high Rayleigh number, large-scale order returns. The LSC reversals become periodic and the fluid CoM moves along an arc-like path, reminiscent of pendulum motion [see Fig. 9(a) for a close-up view]. In this section, we will reconcile this high-Ra behavior with the pendulum structure of Eqs. (58) to (60) that was observed in Section IV.

First, although the large-scale dynamics are orderly at high Rayleigh number, Fig. 8 shows that turbulent fluctuations prevail at the small scales. The snapshot seen in Fig. 8(a) illustrates the small-scale complexity of the temperature field arising in the DNS at $Ra = 1.6 \times 10^9$. To further characterize this state, Fig. 8(b) shows a time-series of the temperature T_0 measured at a fixed location in the annulus. The signal exhibits a dominant oscillatory structure, with period corresponding to the LSC reversals. However, the signal shows significant fluctuations about this periodic oscillation. The frequency power-spectrum of T_0 shown in Fig. 8(c) reveals greater detail. The spectrum peaks at a value f^* corresponding to the main periodic component, and thus the frequency of LSC reversals. At higher frequencies, the spectrum decays with a -1.4 power, consistent with the Bolgiano-Obukhov turbulence scaling of natural convection [59, 60]. These observations not only demonstrate the presence of turbulence at $Ra = 1.6 \times 10^9$, but also confirm that the DNS successfully resolves the turbulent behavior.

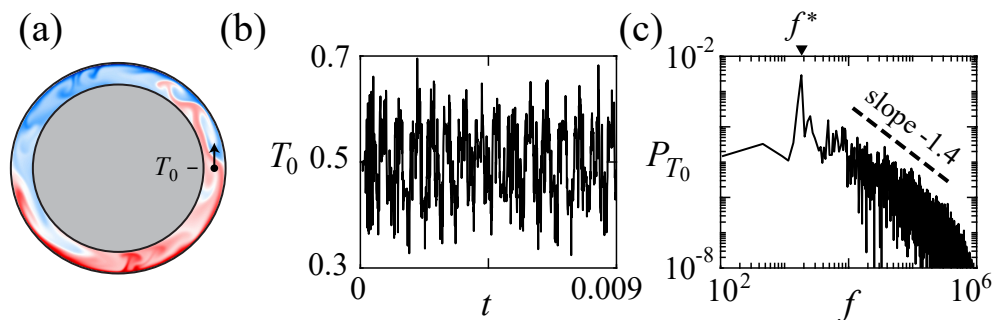


FIG. 8. Temperature measurements reveal the presence of large-scale periodic motion and small-scale turbulent fluctuations. (a) A temperature “probe” is placed at the center of the annular channel, $\theta = 0$, $r = 0.45$. (b) The temperature T_0 measured at the probe shows periodic oscillation in time, with small-scale perturbations due to the turbulent flow field. (c) The power spectrum of T_0 shows the main frequency of oscillation f^* and a power-law decay with exponent -1.4 in the inertial regime of turbulence. Parameter values are $Ra = 1.6 \times 10^9$, $Pr = 4$, and $r_0 = 0.4$.

We now ask whether the dominant frequency, f^* , of LSC reversals in the high-Ra regime can be predicted by the ODE model, Eqs. (58) to (60)? As observed in Section IV, this system corresponds to a damped, driven pendulum with fulcrum $(0, y_1)$, angle $\phi(t)$, mass m , length l , CoM coordinates $(X, Y) = (l \sin \phi, y_1 - l \cos \phi)$, and angular momentum $L = ml^2 \dot{\phi}$. In the following analysis, we identify an energy law satisfied by this pendulum system that leads to accurate estimates of the frequency f^* .

First, the length of the pendulum can generally vary with time $l = l(t)$. Multiplying Eq. (59) by X , Eq. (60) by Y , and adding gives the exact relation

$$\frac{d}{dt} l^2 = -2\beta l^2 + 2\beta \Delta y (Y - y_1), \quad (83)$$

where $\Delta y = y_0 - y_1 > 0$. For the system to reach a limit cycle, the time average of dl^2/dt must vanish, giving the exact relationship

$$\langle l^2 \rangle = \Delta y \langle Y - y_1 \rangle, \quad (84)$$

where $\langle \cdot \rangle$ indicates a time average. This equation offers an immediate observation: the fact that l^2 is non-negative implies that $\langle Y - y_1 \rangle \geq 0$. Hence, in the case of a limit-cycle solution, the average position of the CoM lies above the fulcrum.

Next, to estimate the oscillation frequency it is necessary to solve for l , at least in the mean sense. To this end, we introduce the energy

$$E = \frac{1}{2}kL^2 + \text{RaPr}(Y - y_1). \quad (85)$$

The terms on the right side of Eq. (85) represent kinetic and potential energy respectively. Taking a time derivative, using Eqs. (58) and (60), and simplifying yields the energy law,

$$\dot{E} = -\alpha\text{Pr}kL^2 + \beta\text{RaPr}(y_0 - Y). \quad (86)$$

The first term on the right-hand side represents energy dissipation associated with a non-trivial flow field, $L \neq 0$ (recall Pr is proportional to viscosity). The second term represents positive energy injected into the system by the driving terms with prefactor β in Eq. (60). For a limit cycle to exist, the condition $\langle \dot{E} \rangle = 0$ must hold, giving

$$k\alpha\langle L^2 \rangle = \text{Ra}\beta\langle y_0 - Y \rangle. \quad (87)$$

When this condition is met, the energy lost to dissipation balances the energy injected into the system over a cycle.

Equations (84) and (87) constitute two constraints for the three unknowns $\langle l^2 \rangle$, $\langle Y \rangle$, $\langle L^2 \rangle$. One additional constraint is needed to close the system. To obtain this last constraint, we introduce two assumptions. First, we assume the length l to be nearly constant in time, as is consistent with numerical measurements that will be shown in Fig. 9(a). Second, although Eq. (86) shows that energy is not conserved in general, it is conserved on average for a limit cycle. We will therefore assume the energy to be equal to its average value $E(t) = \langle E \rangle$. Taking the time average of Eq. (85) gives

$$\langle E \rangle = \frac{1}{2}k\langle L^2 \rangle + \text{RaPr}\langle Y - y_1 \rangle. \quad (88)$$

At the bottom of the swing, $Y = y_1 - l$, the angular momentum is near its maximum $L = L_{\max}$, giving energy

$$E_{\text{bot}} = \frac{1}{2}kL_{\max}^2 - \text{RaPr}l. \quad (89)$$

Assuming nearly constant energy, $E_{\text{bot}} = \langle E \rangle$, gives the relationship

$$\text{RaPr}(l + \langle Y - y_1 \rangle) = \frac{1}{2}k(L_{\max}^2 - \langle L^2 \rangle). \quad (90)$$

Naturally, the scales of L_{\max}^2 and $\langle L^2 \rangle$ are directly related. For example, if $L(t)$ varies sinusoidally, then $\langle L^2 \rangle = L_{\max}^2/2$. We therefore set $\langle L^2 \rangle = L_{\max}^2/m$ for some constant m to be chosen later (e.g. $m = 2$ for a sinusoidal wave and $m = 3$ for a triangular wave). Making this substitution in Eq. (90), while using Eq. (87), and simplifying gives

$$2\alpha\text{Pr}(l + \langle Y - y_1 \rangle) = \beta(m - 1)\langle y_0 - Y \rangle. \quad (91)$$

Then inserting Eq. (84) with constant l gives a quadratic equation for l

$$2\alpha\text{Pr}l(\Delta y + l) = \beta(m - 1)(\Delta y^2 - l^2). \quad (92)$$

The quadratic can be factored exactly and possesses one positive root,

$$l = \Delta y \left(\frac{(m - 1)\beta}{(m - 1)\beta + 2\alpha\text{Pr}} \right). \quad (93)$$

We have therefore solved for the pendulum length under the assumptions that a limit cycle has been reached and that the length is nearly constant. The parameter m relates the maximum and RMS values of angular momentum L . Observations from DNS suggest that $L(t)$ lies approximately between a sinusoidal ($m = 2$) and triangular ($m = 3$) waveform; see, for example, the right-most panel of Fig. 2. We will therefore set $m = 2.5$.

If the amplitude of the pendulum motion were small, we could determine the period T_p right away using the well-known formula $T_p = 2\pi\sqrt{l/g}$, where $g = kl^2\text{RaPr}$ for the pendulum system given by Eqs. (58) to (60). Numerical measurements, however, will show the amplitude of motion to be large [see Fig. 9(a)]. In this case, the period is given by the more general formula

$$T_p = \frac{4}{\sqrt{kl\text{RaPr}}} K \left(\sin^2 \frac{\phi_{\max}}{2} \right), \quad (94)$$

where ϕ_{\max} is the maximum angle reached by the pendulum, and $K(x) = \int_0^{\pi/2} (1 - x^2 \sin^2 \theta)^{-1/2} d\theta$ is the complete elliptic integral of the first kind. The value of ϕ_{\max} is thus needed to estimate the period and hence f^* .

At the apex, $\phi = \phi_{\max}$ and $\dot{X} = \dot{Y} = 0$, which upon inserting into Eqs. (59) and (60) and simplifying gives $X^2 = (y_0 - Y)(Y - y_1)$. Inserting the definitions $X = l \sin \phi$ and $Y = y_1 - l \cos \phi$ and solving for l gives the relationship $l = -\Delta y \cos \phi_{\max}$. Some further manipulations then give the argument of the elliptic integral in Eq. (94) as

$$\sin^2 \frac{\phi_{\max}}{2} = \frac{1 - \cos \phi_{\max}}{2} = \frac{\Delta y + l}{2\Delta y} = \frac{(m-1)\beta + \alpha \text{Pr}}{(m-1)\beta + 2\alpha \text{Pr}}, \quad (95)$$

where we have assumed constant l as given by Eq. (93). Inserting this formula into Eq. (94) gives the period of oscillations,

$$T_p = \frac{4}{\sqrt{kl \text{Ra Pr}}} K \left(\frac{(m-1)\beta + \alpha \text{Pr}}{(m-1)\beta + 2\alpha \text{Pr}} \right). \quad (96)$$

The frequency of LSC reversals is then given by $f^* = 1/T_p$.

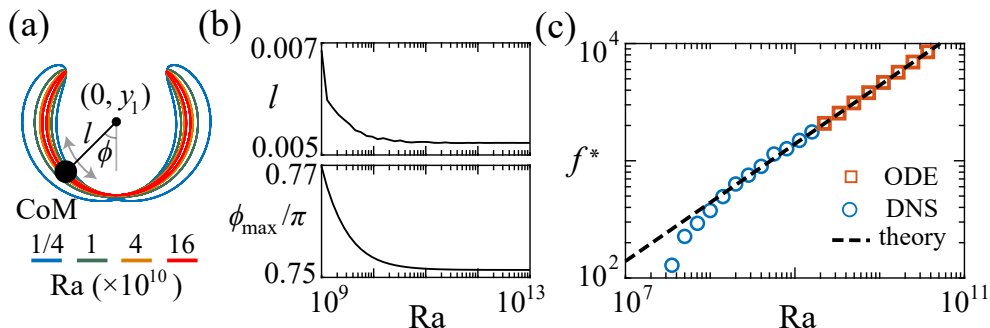


FIG. 9. At high Ra , the fluid CoM oscillates like a mechanical pendulum. (a) The CoM trajectory approaches a circular arc as $Ra \rightarrow \infty$, showing periodic oscillation. (b) The pendulum length l and maximum swing angle ϕ_{\max} each converge to an asymptote as $Ra \rightarrow \infty$. (c) The dominant frequency f^* of LSC reversals measured from DNS and from the ODE model are well predicted by Eq. (96) at high Ra . (a)-(b) and squares in (c) are obtained from the ODE solutions, circles in (c) are from full DNS. All data have $\text{Pr} = 4$ and $r_0 = 0.4$.

Figure 9 shows numerical measurements of the CoM motion in the high- Ra regime in comparison to this prediction. First, Fig. 9(a) shows CoM trajectories computed numerically from Eqs. (58) to (60) for Rayleigh numbers in the range $Ra = 1/4 - 16 \times 10^{10}$. Each trajectory closely resembles the rhythmic swinging of a pendulum about the fulcrum point $(0, y_1)$ that is predicted by Eq. (57). At $Ra = 1/4 \times 10^{10}$ (blue orbit), the pendulum length l varies somewhat over the period. At higher Rayleigh number, though, the orbit tightens and l remains nearly constant throughout the period. This observation is consistent with the assumption of constant l made in the analysis above. Figure 9(b) show measurements of the pendulum length l and maximum swing angle ϕ_{\max} , both of which lie in a relatively narrow range over four decades of Ra . Interestingly, as $Ra \rightarrow \infty$, ϕ_{\max} appears to converge to a value near $3\pi/4$.

Most importantly, Fig. 9(c) shows numerical measurements of the LSC reversal frequency f^* in comparison to the theoretical prediction Eq. (96). The figure shows measurements of f^* taken from both the DNS (blue circles) and from simulation of the ODE system (orange squares), along with the prediction from Eq. (96) with $m = 2.5$ (dashed line). The figure shows that Eq. (96) accurately predicts the LSC reversal frequency over roughly the largest decade of Rayleigh numbers that are practical for DNS. For $Ra > 2 \times 10^9$, the DNS becomes computationally prohibitive, but measurements of f^* from simulations of the ODE model are possible and still agree with the prediction from Eq. (96). The close agreement between DNS, the ODE model, and Eq. (96) suggest that the main mechanism for high- Ra LSC reversals has been properly accounted for. In particular, LSC reversals result from an inertial overshoot of the CoM, directly analogous to a damped, driven pendulum system.

VII. DISCUSSION

In this work, we have examined thermal convection in an annulus using both DNS and a simplified ODE model that derives systematically from the governing equations. In both the DNS and the ODE model, we observe the onset of fluid motion at a critical Rayleigh number Ra_1^* , where flow begins to circulate steadily in one direction, and we observe the transition to chaotic bidirectional flows at a higher critical Rayleigh number Ra_2^* . Stability analysis of the ODE model yields formulas for Ra_1^* and Ra_2^* that accurately predict these transitions with no adjustable parameters, demonstrating a modeling accuracy that has not been achieved previously. Both the DNS and ODE model show a high-Rayleigh number state, in which the bulk flow changes direction periodically despite small-scale turbulent fluctuations in the flow field.

There are still many interesting aspects of this annular convection problem awaiting exploration. First, one surprising observation in Fig. 6 is the existence of a critical Pr^* , below which the circulating state remains stable for arbitrarily

large Ra. For the case shown in Fig. 6, the threshold value $\text{Pr}^* = 0.55$ is below that of common working fluids such as water. However, liquid metal convection [61] is known to have low Pr due to the high thermal conductivity. Thus, future experiments featuring liquid metal could attempt to verify this ever-circulating state. Such experiments, combined with new analysis that builds upon the present theory, could offer insight into thermal transport and potentially novel Nu–Ra scaling relationships associated with the ever-circulating state.

Secondly, in this work, we have examined a fixed annular geometry with $r_0 = 0.4$, but changing the radius of the inner boundary could certainly affect the states of convection. Preliminary inquiries suggest smaller r_0 causes the periodic state to appear over a wider range of Ra. In the limit of $r_0 \rightarrow 0$, the annular geometry tends to a circular domain, which is a canonical case worthy of study. We note that the low-dimensional ODE model discussed here loses accuracy in this limit as a result of the wider channel permitting larger deviations from shear flow. This situation thus presents new modeling challenges for future work.

SUPPLEMENTAL MATERIAL

Supplementary movies are available at <https://math.nyu.edu/~jinzi/research/AnnularConvection/Movie/>.

-
- [1] F. H. Busse, Non-linear properties of thermal convection, *Rep. Prog. Phys.* **41**, 1929 (1978).
 - [2] R. Camassa and S. Wiggins, Transport of a passive tracer in time-dependent rayleigh-bénard convection, *Physica D: Nonlinear Phenomena* **51**, 472 (1991).
 - [3] S. Childress, *An Introduction to Theoretical Fluid Mechanics*, Courant lecture notes in mathematics (Courant Institute of Mathematical Sciences, 2009).
 - [4] G. Ahlers, S. Grossmann, and D. Lohse, Heat transfer and large scale dynamics in turbulent Rayleigh-Bénard convection, *Rev. Mod. Phys.* **81**, 503 (2009).
 - [5] M. McCurdy, N. Moore, and X. Wang, Convection in a coupled free flow-porous media system, *SIAM J. Appl. Math.* **79**, 2313 (2019).
 - [6] M. McCurdy, N. J. Moore, and X. Wang, Predicting convection configurations in coupled fluid-porous systems, *J. Fluid Mech.* **953**, A23 (2022).
 - [7] R. Salmon, *Lectures on Geophysical Fluid Dynamics* (Oxford University Press, 1998).
 - [8] J.-Q. Zhong, D. Funfschilling, and G. Ahlers, Enhanced heat transport by turbulent two-phase Rayleigh-Bénard convection, *Phys. Rev. Lett.* **102**, 124501 (2009).
 - [9] F. F. Araujo, S. Grossmann, and D. Lohse, Wind Reversals in Turbulent Rayleigh-Bénard Convection, *Phys. Rev. Lett.* **95**, 084502 (2005).
 - [10] E. Brown and G. Ahlers, Large-scale circulation model for turbulent Rayleigh-Bénard convection, *Phys. Rev. Lett.* **98**, 134501 (2007).
 - [11] E. van Doorn, B. Dhruva, K. R. Sreenivasan, and V. Cassella, Statistics of wind direction and its increments, *Phys. Fluids* **12**, 1529 (2000).
 - [12] G. A. Glatzmaier, R. S. Coe, L. Hongre, and P. H. Roberts, The role of the Earth’s mantle in controlling the frequency of geomagnetic reversals, *Nature* **401**, 885 (1999).
 - [13] T. D. de Wit, V. V. Krasnoselskikh, S. D. Bale, J. W. Bonnell, T. A. Bowen, C. H. K. Chen, C. Froment, K. Goetz, P. R. Harvey, V. K. Jagarlamudi, A. Larosa, R. J. MacDowall, D. M. Malaspina, W. H. Matthaeus, M. Pulupa, M. Velli, and P. L. Whittlesey, Switchbacks in the Near-Sun Magnetic Field: Long Memory and Impact on the Turbulence Cascade, *Astrophys. J. Suppl. Ser.* **246**, 39 (2020).
 - [14] K. L. Chong, Y. Yang, S.-D. Huang, J.-Q. Zhong, R. J. A. M. Stevens, R. Verzicco, D. Lohse, and K.-Q. Xia, Confined Rayleigh-Bénard, rotating Rayleigh-Bénard, and double diffusive convection: A unifying view on turbulent transport enhancement through coherent structure manipulation, *Phys. Rev. Lett.* **119**, 064501 (2017).
 - [15] A. Belmonte, A. Tilgner, and A. Libchaber, Temperature and velocity boundary layers in turbulent convection, *Phys. Rev. E* **50**, 269 (1994).
 - [16] S. Grossmann and D. Lohse, Scaling in thermal convection: a unifying theory, *J. Fluid Mech.* **407**, 27 (2000).
 - [17] J. J. Niemela, L. Skrbek, K. R. Sreenivasan, and R. J. Donnelly, Turbulent convection at very high Rayleigh numbers, *Nature* **404**, 837 (2000).
 - [18] K. Khazmutdinova, D. Nof, D. Tremaine, M. Ye, and M. N. J. Moore, A minimal model for predicting ventilation rates of subterranean caves, *J. Cave Karst Stud.* **81**, 264 (2019).
 - [19] M. N. J. Moore, Riemann-Hilbert Problems for the Shapes Formed by Bodies Dissolving, Melting, and Eroding in Fluid Flows, *Commun. Pure Appl. Math.* **70**, 1810 (2017).
 - [20] B. Favier, J. Purseed, and L. Duchemin, Rayleigh-Bénard convection with a melting boundary, *J. Fluid Mech.* **858**, 437 (2019).
 - [21] S. Weady, J. Tong, A. Zidovska, and L. Ristroph, Anomalous Convective Flows Carve Pinnacles and Scallops in Melting Ice, *Phys. Rev. Lett.* **128**, 044502 (2022).
 - [22] P. Meakin and B. Jamtveit, Geological pattern formation by growth and dissolution in aqueous systems, *Proceedings of the Royal Society A: Mathematical, Physical and Engineering Sciences* **466**, 659 (2010).
 - [23] L. Ristroph, M. N. J. Moore, S. Childress, M. J. Shelley, and J. Zhang, Sculpting of an erodible body by flowing water, *Proc. Natl. Acad. Sci. U. S. A.* **109**, 19606 (2012).

- [24] M. N. J. Moore, L. Ristroph, S. Childress, J. Zhang, and M. J. Shelley, Self-similar evolution of a body eroding in a fluid flow, *Phys. Fluids* **25** (2013).
- [25] B. D. Quaife and M. N. J. Moore, A boundary-integral framework to simulate viscous erosion of a porous medium, *J. Comput. Phys.* **375**, 1 (2018).
- [26] S.-H. Chiu, M. N. J. Moore, and B. Quaife, Viscous transport in eroding porous media, *J. Fluid Mech.* **893**, A3 (2020).
- [27] N. J. Moore, J. Cherry, S.-H. Chiu, and B. D. Quaife, How fluid-mechanical erosion creates anisotropic porous media, *Physica D* **445**, 133634 (2023).
- [28] M. Maruyama, N. Kuribayashi, K. Kawabata, and J. S. Wettlaufer, Shocks and curvature dynamics: A test of global kinetic faceting in crystals, *Phys. Rev. Lett.* **85**, 2545 (2000).
- [29] J. M. Huang, M. N. J. Moore, and L. Ristroph, Shape dynamics and scaling laws for a body dissolving in fluid flow, *J. Fluid Mech.* **765**, 10.1017/jfm.2014.718 (2015).
- [30] J. M. Huang, J. Tong, M. Shelley, and L. Ristroph, Ultra-sharp pinnacles sculpted by natural convective dissolution, *Proc. Natl. Acad. Sci. U. S. A.* **117**, 23339 (2020).
- [31] J. M. Huang and N. J. Moore, Morphological attractors in natural convective dissolution, *Phys. Rev. Lett.* **128**, 024501 (2022).
- [32] V. Bergeron, C. Berger, and M. D. Betterton, Controlled irradiative formation of penitentes, *Phys. Rev. Lett.* **96**, 098502 (2006).
- [33] P. Claudin, H. Jarry, G. Vignoles, M. Plapp, and B. Andreotti, Physical processes causing the formation of penitentes, *Phys. Rev. E* **92**, 033015 (2015).
- [34] J. A. Whitehead, Moving heaters as a model of continental drift, *Phys. Earth Planet. In.* **5**, 199 (1972).
- [35] J.-Q. Zhong and J. Zhang, Thermal convection with a freely moving top boundary, *Phys. Fluids* **17**, 115105 (2005).
- [36] J. A. Whitehead and M. D. Behn, The continental drift convection cell, *Geophys. Res. Lett.* **42**, 4301 (2015).
- [37] J. M. Huang, J.-Q. Zhong, J. Zhang, and L. Mertz, Stochastic dynamics of fluid–structure interaction in turbulent thermal convection, *J. Fluid Mech.* **854** (2018).
- [38] N. J. Moore and J. M. Huang, Fluid pendulum explains reversals of the large-scale circulation in thermal convection, *arXiv:2307.13148* (2023).
- [39] D. J. Tritton, *Physical Fluid Dynamics*, Oxford Science Publ (Clarendon Press, 1988).
- [40] K. Sugiyama, R. Ni, R. J. A. M. Stevens, T. S. Chan, S.-Q. Zhou, H.-D. Xi, C. Sun, S. Grossmann, K.-Q. Xia, and D. Lohse, Flow reversals in thermally driven turbulence, *Phys. Rev. Lett.* **105**, 034503 (2010).
- [41] R. Ni, S.-D. Huang, and K.-Q. Xia, Reversals of the large-scale circulation in quasi-2D Rayleigh–Bénard convection, *J. Fluid Mech.* **778**, R5 (2015).
- [42] J. J. Niemela and K. R. Sreenivasan, Rayleigh-number evolution of large-scale coherent motion in turbulent convection, *Europhys. Lett.* **62**, 829 (2003).
- [43] Y. Wang, P.-Y. Lai, H. Song, and P. Tong, Mechanism of large-scale flow reversals in turbulent thermal convection, *Sci. Adv.* **4**, 7480 (2018).
- [44] H. F. Creveling, J. F. D. Paz, J. Y. Baladi, and R. J. Schoenhals, Stability characteristics of a single-phase free convection loop, *J. Fluid Mech.* **67**, 65 (1975).
- [45] J. L. Kaplan and J. A. Yorke, Preturbulence: A regime observed in a fluid flow model of Lorenz, *Comm. Math. Phys.* **67**, 93 (1979).
- [46] J. Singer, Y.-Z. Wang, and H. H. Bau, Controlling a chaotic system, *Phys. Rev. Lett.* **66**, 1123 (1991).
- [47] M. Gorman, P. J. Widmann, and K. A. Robbins, Chaotic flow regimes in a convection loop, *Phys. Rev. Lett.* **52**, 2241 (1984).
- [48] B. Futterer, A. Brucks, R. Hollerbach, and C. Egbers, Thermal blob convection in spherical shells, *Int. J. Heat Mass Transfer* **50**, 4079 (2007).
- [49] M. Gorman, P. J. Widmann, and K. A. Robbins, Nonlinear dynamics of a convection loop: A quantitative comparison of experiment with theory, *Physica D* **19**, 255 (1986).
- [50] T. Y. Hou and R. Li, Computing nearly singular solutions using pseudo-spectral methods, *J. Comput. Phys.* **226**, 379 (2007).
- [51] R. Peyret, *Spectral methods for incompressible viscous flow*, Vol. 148 (Springer Science & Business Media, 2002).
- [52] J. M. Huang, M. J. Shelley, and D. B. Stein, A stable and accurate scheme for solving the Stefan problem coupled with natural convection using the Immersed Boundary Smooth Extension method, *J. Comput. Phys.* **432**, 110162 (2021).
- [53] J. M. Huang and J. Zhang, Rayleigh–Bénard thermal convection perturbed by a horizontal heat flux, *J. Fluid Mech.* **954**, 10.1017/jfm.2022.1035 (2022).
- [54] A. J. Majda, M. N. J. Moore, and D. Qi, Statistical dynamical model to predict extreme events and anomalous features in shallow water waves with abrupt depth change, *Proc. Natl. Acad. Sci. U. S. A.* **116**, 3982 (2019).
- [55] N. J. Moore, C. T. Bolles, A. J. Majda, and D. Qi, Anomalous waves triggered by abrupt depth changes: Laboratory experiments and truncated KdV statistical mechanics, *J. Nonlinear Sci.* **30**, 3235 (2020).
- [56] H. Sun and N. J. Moore, On Normal and Non-Normal Wave Statistics Implied by a Canonical–Microcanonical Gibbs Ensemble of the Truncated KdV System, *J. Statist. Phys.* **190**, 4 (2023).
- [57] H. Sun, N. J. Moore, and F. Bao, Parameter Estimation for the Truncated KdV Model through a Direct Filter Method, *Journal of Machine Learning for Modeling and Computing* **4** (2023).
- [58] E. Ott, *Chaos in Dynamical Systems* (Cambridge university press, 2002).
- [59] X.-Z. Wu, L. Kadanoff, A. Libchaber, and M. Sano, Frequency power spectrum of temperature fluctuations in free convection, *Phys. Rev. Lett.* **64**, 2140 (1990).
- [60] D. Lohse and K.-Q. Xia, Small-scale properties of turbulent Rayleigh–Bénard convection, *Annu. Rev. Fluid Mech.* **42**, 335 (2010).
- [61] L. Ren, X. Tao, L. Zhang, M.-J. Ni, K.-Q. Xia, and Y.-C. Xie, Flow states and heat transport in liquid metal convection, *J. Fluid Mech.* **951**, R1 (2022).